Continuous flow synthesis of yttria-stabilized-zirconia nanocrystals in supercritical solvothermal conditions

Yoan Denis, Catherine Elissalde, Matthew R. Suchomel, Marion Gayot, François Weill, Christine Labrugère, Laetitia Étienne, Mélanie Vaudescal, Nithavong Cam, U-Chan Chung, et al.

ADVANCED MATERIALS TECHNOLOGIES
www.advmattechnol.de

Continuous Flow Synthesis of Yttria-Stabilized-Zirconia Nanocrystals in Supercritical Solvothermal Conditions

*Yoan Denis, Catherine Elissalde, Matthew R. Suchomel, Marion Gayot, François Weill, Christine Labrugère, Laetitia Etienne, Mélanie Vaudesca, Nithavong Cam, U-Chan Chung, Helen Reveron, Jérome Chevalier, Thomas Hérisson de Beauvoir, Claude Estournès, Cyril Aymonier, Graziella Goglio, and Gilles Philippot**

The synthesis of yttria-stabilized zirconia nanoparticles with a fine control on the chemical composition and the distribution of yttrium cations is of major interest to master the mechanical, optical or ionic conduction properties of the final material. However, a fine control of this chemical homogeneity within the particles, especially above 5 mol.% of yttria (Y_2O_3), is challenging with conventional synthesis routes. In the present study, for the first time the interest of using supercritical sol–gel like synthesis is demonstrated for the continuous production in a single step of high quality zirconia (ZrO_2) nanocrystals of 7 nm stabilized with Y_2O_3 without post-treatment. Three compositions are investigated, i.e., 1.5, 3, and 8 mol.% of Y_2O_3 and in-depth physico- chemical characterizations such as X-ray diffraction, total X-ray scattering, High-resolution electron microscopy, Raman and X-ray photoelectron spectroscopy are performed to asses and thus prove the successful synthesis of these different compositions while keeping a good chemical homogeneity. This enables to confirm that this original process leads to a unique and fine structural control for such small yttria-doped zirconia nanocrystals.

1. Introduction

Given its functional properties and its key role in a diverse range of applications, from thermal barrier coatings to biomedical devices, there is a significant and long-standing interest on yttria-stabilized zirconia. In this ceramic material, an intricate three-way interplay of atomic structure, microstructure, and physical properties is choreographed by the details of different possible synthetic routes. Among the three common phases of pure zirconia, the monoclinic phase is the most stable at low temperatures (< ≈1000 °C), whereas the tetragonal phase becomes stable at intermediate temperatures (until ≈2350 °C) and the cubic phase at higher temperatures until melting (≈2700 °C).[1] Using dopants such as yttria, magnesia or ceria allows to play with transformation temperatures

Y. Denis, C. Elissalde, M. R. Suchomel, M. Gayot, F. Weill, C. Labrugère, L. Etienne, M. Vaudesca, N. Cam, U-C. Chung, C. Aymonier, G. Goglio, G. Philippot
Univ. Bordeaux
CNRS
Bordeaux INP
UMR5026
ICMCB
Pessac F-33600, France
E-mail: gilles.philippot@icmcb.cnrs.fr

H. Reveron, J. Chevalier
Univ Lyon
INSA Lyon
UCBL
CNRS
UMR5510
MATEIS
20 Avenue Albert Einstein, Villeurbanne F-69621, France

T. H. de Beauvoir, C. Estournès
CNRS-INP-UPS
Université Toulouse 3 – Paul Sabatier
CIRIMAT
118 route de Narbonne, Toulouse 31062, France

The ORCID identification number(s) for the author(s) of this article can be found under https://doi.org/10.1002/admt.202301474

DOI: 10.1002/admt.202301474

and keep high-temperature phases after sintering. In particular, the incorporation of yttrium in the zirconia lattice, as a solid solution has been the most efficient strategy to decrease the tetragonal-to-monoclinic (t–m) transformation temperature. In particular, zirconia stabilized with 1.5 to 3 mol.% yttria (generally referred as 1.5- and 3Y-ZrO_2) can exhibit mostly tetragonal grains after sintering, but transform toward the monoclinic stable phase under stress. This is widely exploited to obtain excellent mechanical properties through a phase-transformation toughening mechanism.[2] On the other side and for different applications or products, the cubic phase can be favored and necessitates higher yttria contents, since it plays an important role on the optical and/or ionic conduction properties.[3] In addition to the stabilizer content, microstructural parameters, such as the grain size and homogeneity of yttria in the grains play a pivotal role in the stability of the tetragonal and cubic phases.[3] Lowering sintering temperatures is for example important to keep the tetragonal phase in zirconia ceramics with a low yttria content, which needs ultrafine starting powders.[4,5] In this context, the capability to control the production of nano-powders of the different polymorphs of stabilized ZrO_2 and / or mixture of them becomes the key to optimize the final ceramic property. Therefore, the understanding and mastering of the formation/crystallization mechanisms involved during a given synthesis is thus fundamental to meet the expected crystal structure, in particular metastable tetragonal or cubic phases. A wide range of synthesis methods for the production of zirconia nanoparticles have been explored and reported,[6] among the synthesis routes that target the production of pure and tetragonal metastable zirconia nanoparticles (i.e., chemical vapor deposition, combustion methods, sol–gel, co-precipitation and solvothermal), sol–gel and solvothermal methods present great advantages in terms of control over the particle size and distribution, purity and composition homogeneity.[7] For instance, the synthesis of undoped metastable tetragonal ZrO_2 polymorph associated with a fine control over the nanoparticle size and size distribution is particularly attractive for optimizing the mechanical properties if these powders are later sintered into dense and nanostructured ceramics at relatively low temperatures (below that of t-m transformation).[8] Given that the tetragonal phase is not thermodynamically stable at room temperature, several influencing factors are considered to provide explanations for this meta-stabilization, including the nature and concentration of the precursors, the types of solvents, the use of dopants, the surface chemistry (use of surfactants), the nanocrystal sizes, the role of hydroxyls and oxygen vacancies, the contributions of surface energy and the lattice strain.[9] Focusing on the continuous supercritical solvothermal process, a versatile synthesis method known for its "sustainable character",[10] the production of metal oxide nanocrystals in a single step has been largely demonstrated over the last 30 years,[11] and more specifically in the case of zirconia.[12–16] It was recently highlighted its capability to produce undoped tetragonal zirconia nanocrystals, in this work, Auxéméry et al.[17] have clearly shown that the size of ZrO_2 nanocrystals cannot be the only determining factor in the stabilization at room temperature of the tetragonal phase. Indeed, a comparative study between various synthesis conditions in flow, i.e., hydrothermal method in supercritical water, sol–gel method in a supercritical ethanol–water mixture, and a borderline non-hydrolytic sol–gel route in supercritical ethanol, showed that the ratio of monoclinic over tetragonal phases strongly depends on the amount of water present in the reaction media during the synthesis. The authors demonstrated the possibility of producing ZrO_2 nanocrystals with a constant size of ≈5 nm while tuning the amount of tetragonal phase from 0 up to 90 wt%. The importance of these results is that they strongly call into question the notion of a "critical size" below which 100% of pure tetragonal phase can be meta-stabilized. Instead, they highlighted the key role of water quantity within the synthesis media and more precisely the ability of ethanol to dehydrate in these synthesis conditions, generating water in situ in order to trigger the nucleation and growth of the ZrO_2 nanocrystals.[18] Varying the amount of released water in situ is believed to directly influence the quantity of oxygen vacancies formed within the ZrO_2 nanocrystals first leading to the stabilization of the tetragonal phase. The tetragonal zirconia stabilization controlled by the level of oxygen vacancies and the associated structural disorder is suggested by static and dynamic simulations.[19] In the specific case of zirconia stabilized systems, oxygen vacancies are also involved in the charge compensating mechanism associated with the introduction of dopant such as yttria (Y_2O_3, as tetravalent Zr^{4+} is substituted by trivalent Y^{3+}). The control of the dopant content allows to stabilize either the tetragonal phase or even the cubic one. In the literature, most of the yttria-stabilized ZrO_2 nanoparticles prepared by hydrothermal syntheses are obtained from nitrate precursors. The yttrium content varies from 3 up to 22 mol.% (i.e., 1.5 to 11 mol% of Y_2O_3) and the particle size remains lower than 10 nm.[16] In the case of yttria-stabilized tetragonal zirconia (Y-TZ), the content and distribution of dopant are influencing three crucial phenomena: i) the transformation toughening due to the stress induced by the martensitic transformation of the metastable tetragonal phase toward the monoclinic one, ii) the low temperature degradation (LTD) resulting from the spontaneous t-m transformation in a humid environment and iii) the birefringence of the crystal and by consequence the optical properties such as translucency.[3,4,20,21] If the phase transformation toughening is at the origin of the superior mechanical properties, the LDT is detrimental. Increasing the yttria content decreases the susceptibility of Y-TZ to LTD and improves translucency, but it may be at the expense of strength. There is therefore always a compromise between transformation toughening, LTD resistance, and translucency (or for other applications ionic conductivity).[22] However, this trade-off can be modified through microstructural and structural optimization. In particular, a fine control of the spatial distribution of the dopant and concentration within each particle is a prerequisite to obtain ceramics with optimized properties. Therefore, it must begin from the initial stage of the synthesis, which can be challenging in sub- and supercritical hydrothermal syntheses of yttria-stabilized zirconia when the Y_2O_3 content reaches 8 mol.% (8Y-ZrO_2).[23]

In the present work, the controlled synthesis of high quality yttria-stabilized zirconia nanocrystals is reported. The sol–gel like route in supercritical fluid conditions was used to target a continuous flow synthesis of nanocrystals in one step at 400 °C while controlling both the content/distribution of dopant together with a high degree of selectivity regarding the obtained zirconia polymorphs (i.e., tetragonal and/or monoclinic). Three compositions were studied, i.e., 1.5, 3 and 8 mol.% of Y_2O_3 (1.5Y-ZrO_2, 3Y-ZrO_2, and 8Y-ZrO_2, respectively), with a special emphasis on the

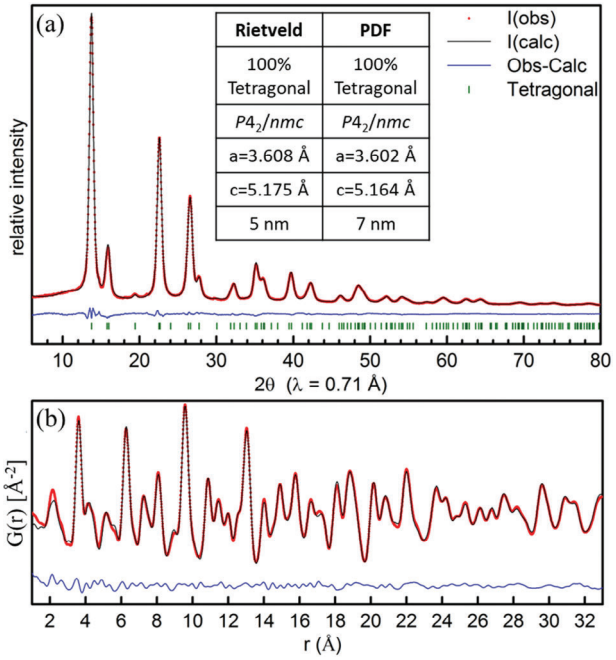

Figure 1. Fits of Mo-source X-ray scattering data measured on the 3Y-ZrO_2 powder a) Rietveld refinement of as-measured Mo-PXRD data and b) small-box fitting of the real space Pair Distribution Function data. Both plots display the Y_{obs} (black points), Y_{calc} (red line), and fit difference curve (blue line). For the Rietveld fit vertical phase tick marks indicate the position of Bragg reflections for tetragonal phase. The inset table summarizes key refined parameters.

chemical and structural characterizations of the 3Y-ZrO_2 powders where 100% tetragonal nanocrystals of 7 nm were produced. The investigations conducted on the two others compositions, i.e., 1.5Y-ZrO_2 and 8Y-ZrO_2 underlined the high level of control that can be reached using supercritical solvothermal synthesis processes in terms of chemical homogeneity even for nanocrystals with sizes below 10 nm.

2. Results and Discussion

2.1. Supercritical Solvothermal Synthesis of 3 mol.% Y_2O_3 – ZrO_2 (3Y-ZrO_2)

2.1.1. Structural and Microstructural Analysis

Rietveld refinement fit profiles of Mo-source Powder X-ray diffraction (Mo-PXRD) data measured on the 3Y-ZrO_2 powder is plotted in **Figure** 1a. The good match between the measured and calculated Mo-PXRD pattern shows that the structure of the 3Y-ZrO_2 powder is well modelled by a $P4_2/nmc$ tetragonal structure of ZrO_2 in agreement with previous reports.[24]

Significant broadening of the Bragg peaks is the result of a nanoscale crystalline domains, which are estimated to be≈5 nm based on the integral breath-microstructure model. Broadening results in overlapping peak profiles that makes it difficult to visually distinguish certain reflections of the tetragonal ZrO_2 structure. However, the excellent counting statistics and low background of this Mo-source measurement clearly demonstrate the absence of any reflections associated with a monoclinic phase, many of which are well-separated in 2θ position and would be discernible if present. On the other hand, for nanoscale powders, the distinction between tetragonal and cubic polymorphs of ZrO_2 by Cu-PXRD is really tricky.

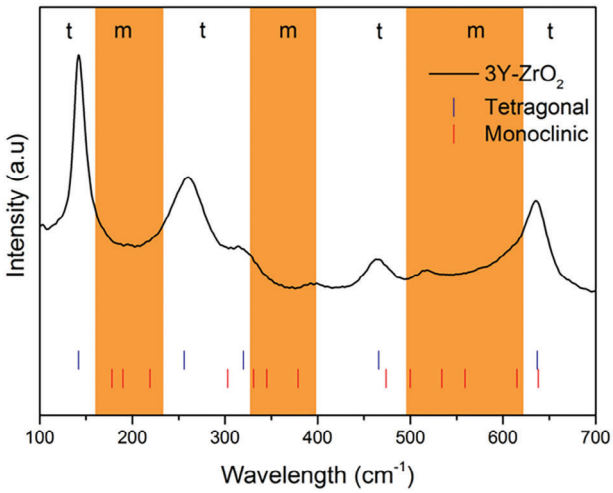

Figure 2. Raman spectra of 3Y-ZrO_2 powder collected at room temperature in the 100–700 cm^{-1} domain. The monoclinic (m) and tetragonal (t) are separated by the orange areas and t- and m-ZrO_2.

In order to more carefully examine the atomic structure of this solvothermal synthesized powder, a total X-ray scattering Pair Distribution Function (PDF) approach was used. Compared with Mo-PXRD Rietveld refinements, PDF analysis provides additional information on the local atomic order and a complementary evaluation of crystallite domain sizes. Figure 1b presents the obtained G(r) function for the 3Y-ZrO_2 powder, and shows the excellent agreement between measured and calculated data when fitting with a single tetragonal $P4_2/nmc$ type structure. The insert in Figure 1a, lists a summary of key refined parameters from the Rietveld and PDF fits, including cell parameters and average crystallite domain size with a good agreement. Compared to Rietveld results, the PDF estimated crystallite size was slightly larger (i.e., 7 nm). Overall, these structural analyses show the crystallization of only the tetragonal structure and demonstrate the nanoscale structural nature of the 3Y-ZrO_2 nanoparticles obtained by a single step sol–gel route under supercritical conditions.

Raman spectroscopy also provided further structural characterization of the 3Y-ZrO_2 powder both for local crystal structure and local disorders. The Raman spectra shown in **Figure 2** clearly corroborate the synthesis of 100% tetragonal 3Y-ZrO_2 nanocrystals. No bands corresponding to the monoclinic polymorph were observed, especially the two intense bands at 178 and 190 cm^{-1} characteristic of this structure. Instead, all the characteristic bands of the tetragonal structure are clearly visible (140, 260, 466, and 637 cm^{-1}).[25]

At this stage, Raman analysis seems to be in agreement with the previous observations made from Mo-PXRD and PDF confirming the synthesis of 100% tetragonal 3Y-ZrO_2 nanocrystals. This result is noteworthy because, even if this is theoretically what should be obtained based on the ZrO_2 – Y_2O_3 phase diagram,[26] this is not the case for the commercial reference

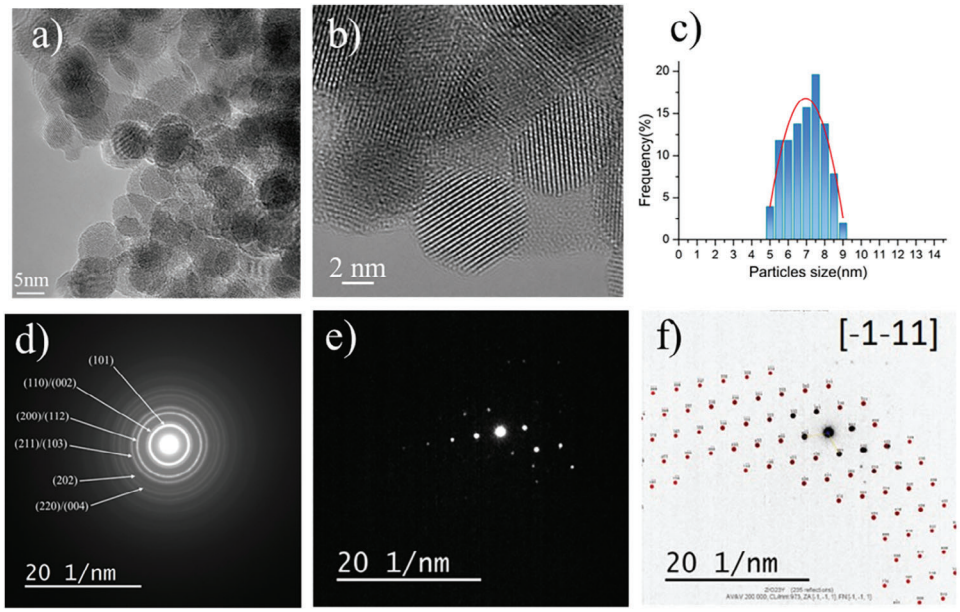

Figure 3. a) HRTEM of several particles b) HRTEM focus on a single 3Y-ZrO_2 particles, c) Size distribution of 3Y-ZrO_2 particles. d) SAED of 3Y-ZrO_2 particles, e) Nanodiffraction on one single 3Y-ZrO_2 nanocrystal, f) indexation of the nanodiffraction pattern with a 4.1° of misorientation. All the indexations are done with the X-ray cell.

(see Figure S1, Supporting Information). A possible explanation of the presence of monoclinic phase content in powders could be due to lack of chemical homogeneity within the powders, which does not happen with the supercritical sol–gel like approach.

High-Resolution Transmission Electron Microscopy (HRTEM) image at low magnification of the 3Y-ZrO_2 nanoparticles is shown in **Figure** 3a. This image provides an indication of the state of aggregation of nanoparticles, which is anticipated with regard to their size, the fact that they are not functionalized and also because they were dried after the synthesis. Higher magnification (Figure 3b) allows to observe fully crystallized nanoparticles with quasi-spherical shape. Atomics plans are going from part to part of particles without any presence of amorphous shell around the particles. An average particle size of 7 ± 1 nm was estimated (Figure 3c). This result is in good agreement with the crystallite size of 5 nm (estimated from Rietveld refinement) and of 7 nm (estimated from PDF). The Selected Area Electron Diffraction (SAED) pattern obtained on a large number of particles is consistent with the tetragonal symmetry of 3Y-ZrO_2 nanocrystals. A nanodiffraction pattern obtained on one single nanocrystal was indexed using the same tetragonal structure used to model Mo-PXRD data (i.e., space group $P4_2/nmc$). There, a misorientation relative to the zone axis was estimated at 4.1° (Figure 3d–f). All these information enable to claim the synthesis of tetragonal 3Y-ZrO_2 nanocrystals without any amorphous shell present at their surface. The high degree of crystallinity within the starting particles is of main importance toward the properties of the ceramics after sintering, as any residual amorphous phase would crystallize into monoclinic phase during the thermal process, depending on its composition and the parameters of the sintering cycle.

Based on these observations we can conclude that we successfully synthesized fully crystalized tetragonal yttria-stabilized zirconia nanoparticles, of 7 nm diameter size, in a single step. Such results could indicate that solvothermal supercritical synthesis leads to a more homogeneous distribution of yttrium compared to other routes applied for the synthesis of commercial 3Y-TZ powders, where a mixture of tetragonal and monoclinic phases is generally observed. The next step is thus to assess this assumption, evaluating the yttria content and its homogeneity within the particles.

2.1.2. Distribution of Yttrium Cations

The Energy Dispersive X-ray Spectroscopy (EDS) elemental mapping of yttrium and zirconium performed on a representative number of 3Y-ZrO_2 nanoparticles (corresponding Scanning Transmission Electron Microscopy image shown on **Figure** 4a) reveals a very homogeneous distribution of yttrium within the particles (Figure 4b,c). Nevertheless, the overlapping of EDS peaks and a lack of intensity for those of yttrium did not allow a proper quantification of the Y/Zr ratio. In order to determine this ratio, a semi-quantitative chemical analysis was performed by X-ray Photoelectron Spectroscopy (XPS), making sure to have eliminated any carbon pollution from the surface beforehand. Indeed, using alkoxide based precursors, it is common to have a carbon contamination at the surface of the particles due to their decomposition in supercritical conditions. To do this, deep etching (≈72–81 nm) was carried out in situ until reaching the compositional plateau (Figure 4d), thus being able to ensure that the measurements correctly represent the composition of the particles. This analysis being semi quantitative, the same analysis was also conducted on the commercial 3Y-TZ commercial powder used as a reference. An atomic percentage of yttrium of 2.1 at.% was obtained in the case of the 3Y-ZrO_2 powder produced in

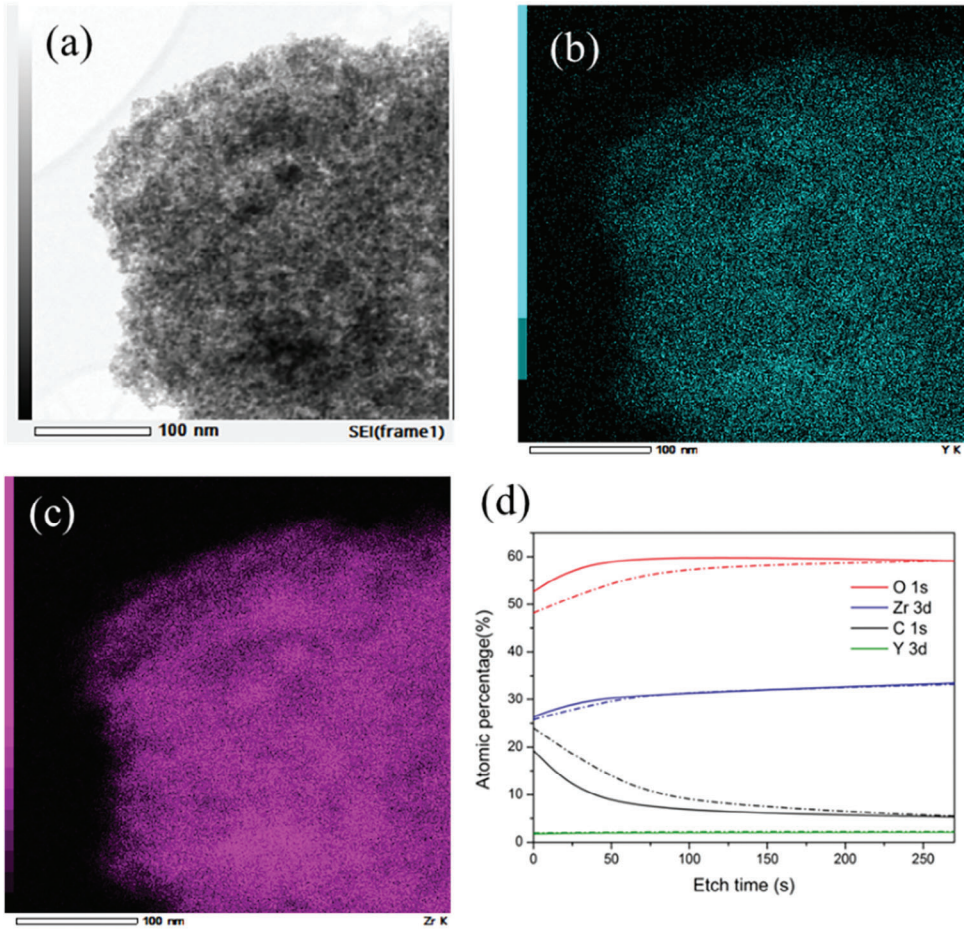

Figure 4. EDS mapping obtained in HRTEM with a) the analyzed area, b) the yttrium mapping c) the zirconium mapping and d) XPS depth profiles (at.%) for the supercritical powder (full line) and commercial powder (dashed line).

supercritical flow conditions, which corresponds to 3.1 mol.% of Y_2O_3, whereas it was of 2.3 at.% (i.e., 3.4 mol.% of Y_2O_3), in the case of the commercial powder (see Supporting Information for details on the calculation). These similar semi-quantitative results show that a precise control of the Y/Zr ratio can be achieved in 3Y-ZrO_2 particles synthesized under supercritical conditions.

Based on our expertise in the field of supercritical sol-gel like flow synthesis of metal oxides, and more specifically of barium titanate based nanoparticles ($Ba_{1-x}SrTi_{1-y}Zr_yO_3$ with $0 \leq x \leq 1$ and $0 \leq y \leq 1$) through a similar synthesis procedure (i.e., from alkoxide precursors mixed in absolute ethanol),[27–31] it is believed that during the solvothermal supercritical synthesis of 3Y-ZrO_2, pre-nucleation clusters are formed in solution where cations of Zr^{4+} and Y^{3+} are homogeneously distributed. Then, the burst nucleation characteristic of the supercritical sol-gel like synthesis (in only few seconds) prevent any demixion of these clusters and form high-quality nanocrystals with a good chemical homogeneity.

Gathering these informations, we can claim that the produced yttria-stabilized zirconia nanocrystals have the expected yttria content (i.e., 3 mol.% of Y_2O_3) and yttrium cations are homogeneously distributed. The next step is to look at the surface chemistry of these particles.

2.1.3. Particle Surface Chemistry

Several factors affect the stability and transformability of the 3Y-TZ tetragonal phase under temperature variations, stress application and/or in humid environment. Among them, the grain size and the concentration of the stabilizing agent or dopant are probably the most important. In the case of yttrium, the meta-stability of the tetragonal phase is linked to the presence of oxygen vacancies which also play a crucial role in the aging phenomenon. The kinetics of zirconia polymorphic transformation during thermal treatments (sintering) or hydrothermal treatments (aging) is also closely related to the presence of surface/lattice hydroxyl defects leading to different phenomena such as de-hydroxylation, hydroxyl migration, surface reconstruction.[32] It is thus essential to make sure that as-produced nanocrystals meet the expectations, especially in terms of chemical homogeneity or repartition of yttrium but also of surface/lattice group's characteristics. Further characterization of the surface then becomes important, especially if one wants to understand the effect of certain surface groups on the meta-stability of the tetragonal phase.

In the as-synthesized 3Y-ZrO_2 powders, -OH and -COO groups were detected in FTIR spectra as shown in **Figure 5**a. The —CH_2 and —CH_3 stretching vibrations are visible in the region

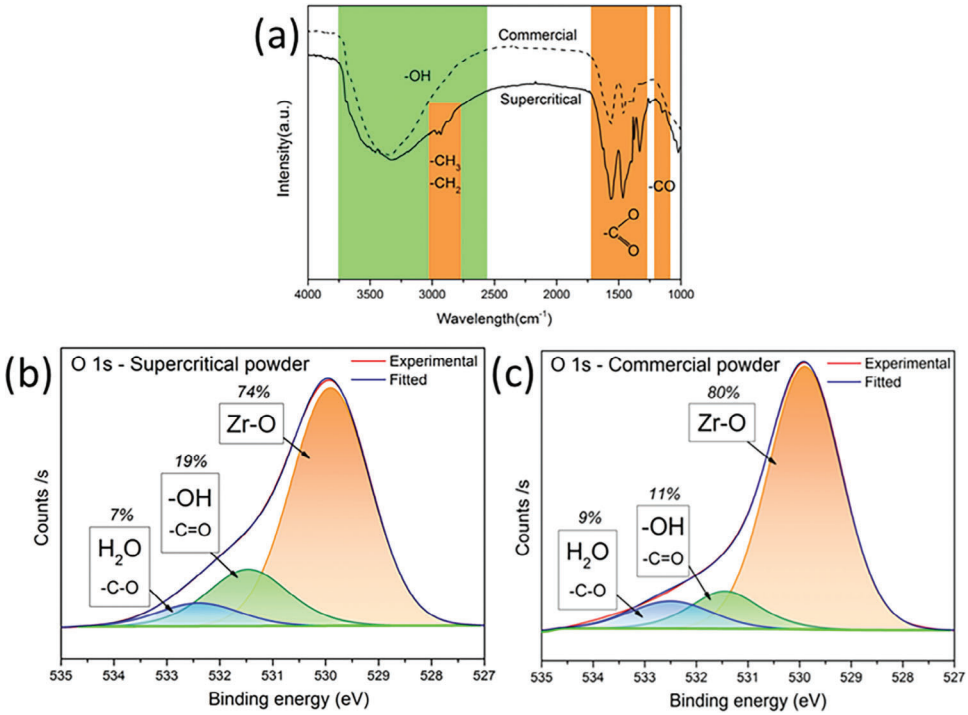

Figure 5. a) Infrared spectroscopy spectra of the 3Y-ZrO_2 particles in the 4000–100 cm^{-1} range, O_{1s} XPS fitting at the top surface of b) supercritical 3Y-ZrO_2 and c) commercial 3Y-TZ powder.

2970–2800 cm^{-1} and the antisymmetric and symmetric vibrations of the carboxylate groups —COO at 1560 and 1460 cm^{-1} are observed. These vibrations bands are characteristics of a chelating bidentate type interaction between the carboxylate function from the precursor decomposition and the metal oxide surface. Moreover, a weak —CO band can be observed at 1020 $cm^{-1}$and in the 3700–3000 cm^{-1} region, a strong band corresponding to —OH groups is detected. These findings are in agreement with the results of a previous work on supercritical solvothermal synthesis.[17]

The O_{1s} XPS fitting (top surface peak) was set considering three contributions, Zr-O from the lattice (529.9 eV), OH/C═O bonds at 531.5 eV and H_2O/C-O ones ≈532.4 eV. For the supercritical 3Y-ZrO_2 powder (Figure 5b), the contribution of lattice structural O^{2-} is estimated at 74%, the OH/C═O one at 19% and the H_2O/C—O ones at 7%. The C—O and C═O bonds are explained by some remaining carbonyl or carboxylate groups. These results demonstrate the presence of —OH groups on the top surface of particles with some remaining —COO groups. In comparison, the commercial reference powder (Figure 5c) leads to proportions of 80% (lattice structural O^{2-}), 11% (OH/C═O) and 9% (H_2O/C—O). Considering this last H_2O/C—O signal quite similar for both powders, it can be observed that the particles obtained by supercritical synthesis had a richer —OH surface than the commercial ones. This effect can be related to the higher specific surface area of the supercritical particles and/or to the fact that commercial particles produced by conventional sol–gel synthesis required the calcination of the gel to promote the crystallization of zirconia. Hence, such an additional thermal treatment can modify the surface chemistry, removing surface species. Hence, those surface chemistry results highlight the potentiality of the supercritical fluids to synthesize highly reactive zirconia nanoparticles that could be exploited as "raw materials" for low temperature sintering processes or for catalysis.[5,33,34]

This first section demonstrates we were able to synthesize in a single step tetragonal yttria-stabilized zirconia spherical nanocrystal, 7 nm in diameter, where the Y_2O_3 content was precisely controlled and homogeneously distributed among the particles. We also showed that with a single step synthesis approach, where there is no post calcination treatment, the surface chemistry of the particles is different compare to what observed on commercial powders. Although there is a non-negligible carbon contamination (which is also the case in the commercial powder), there is a higher density of surface —OH that could impact the reactivity of the material. In the next section we will investigate the reliability of this synthesis process varying the yttria content.

2.2. Supercritical Solvothermal Flow Synthesis of 1.5 mol.% Y_2O_3-ZrO_2 (1.5Y-ZrO_2) and 8 mol.%Y_2O_3-ZrO_2 (8Y-ZrO_2)

2.2.1. Varying the Yttrium Content

As presented in the introduction section, the intimate and complex dependence between the particles size, the quantity of yttria stabilizer and its distribution within the particles often imposes to find compromises in particular to adjust the ceramics' mechanical and optical properties (translucency). The tradeoffs that have to be found are very well illustrated in the work of E. Roteiro et. al.[35] Increasing the quantity of yttrium allows to stabilize the cubic zirconia phase that presents the advantage of having an isotropic refractive index in favor of material

transparency. However, the non-transformability of the cubic phase is detrimental for mechanical properties because of the absence of phase transformation toughening.[2] O. Akhlaghi et al. have shown in the case of the 3Y-TZ ceramics, the higher densification while retaining a very fine grain size (i.e of 50 nm) leads to an improvement of the transparency.[4] The benefit of using such nanometric powders with perfectly controlled composition as raw materials is justified by the very fine control in terms of such size/composition couple that is required.[4] Beyond the 3Y-ZrO_2 and 8Y-ZrO_2 compositions whose interest for applications is not to be reminded anymore, the composition corresponding to 1.5Y-ZrO_2 has recently been highlighted in reason of a promising trade-off between toughness and aging resistance, resulting from the combination of ultrafine grain size and low yttrium content. These ceramics were prepared from 1.5Y-ZrO_2 particles obtained from aqueous colloidal suspensions of nanozirconia containing 0.7 wt% of Al_2O_3. The explanation that has been put forward is based on having i) a highly transformable tetragonal phase, ii) a lower content of oxygen vacancies and iii) the presence of Al_2O_3. These recent results have motivated our interest in the synthesis of nanoparticles of zirconia containing relatively low yttrium content in order to promote a higher t–m transformability in nanostructured ceramics without compromising LTD resistance.

On the basis of these considerations, the two compositions 1.5Y-ZrO_2 and 8Y-ZrO_2 were synthesized by using the same sol–gel like process under supercritical conditions as for 3Y-ZrO_2. The choice of these compositions leads to several challenging questions:

- Is it possible to control the insertion of a very small amount of yttrium (i.e., 1.5 mol. % of Y_2O_3) and to ensure the metastability of the tetragonal phase or is the expected tetragonal/monoclinic ratio is obtained;
- Is it possible to stabilize the cubic phase within the 8Y-ZrO_2 nanocrystals, i.e., can the lattice accommodate the rate of associated oxygen vacancies?

After in situ elimination of any carbon surface pollution, a semi-quantitative evaluation of the Y_2O_3 content of the two powders was performed using XPS (**Figure 6**).

An yttria concentration of 1.8 ± 0.2 mol.% and 8.9 ± 0.9 mol.% was obtained for 1.5Y-ZrO_2 and 8Y-ZrO_2 powders produced in supercritical flow conditions. While the 1.5Y-ZrO_2 powder presents a quantity of Y_2O_3 in good agreement with the targeted value, the 8Y-ZrO_2 powder tends to have a higher concentration of yttria than that expected. This is probably linked to the yttrium precursor used, yttrium 2-methoxyethoxide solution, which has a 15–20 wt% concentration. This nominal concentration given by the supplier being not enough precise, this affects the precision of the real yttrium quantity present within the nanocrystals. This uncertainty having a greater impact for the highest yttrium content.

2.2.2. Microstructural Analysis

HRTEM image is presented for the 1.5Y-ZrO_2 particles in **Figure** 7a. As for 3Y-ZrO_2, the particles are spherical-shaped and fully crystallized. Moreover, a narrow size distribution is also observed for this composition, with an average size of 7 ± 1 nm, similar to the size estimated in the 3Y-ZrO_2 (Figure 7b). However, the particle size distribution seems to be a little wider for 1.5Y-ZrO_2 since particles ranging from 5 to 11 nm were observed (this range was of 5–9 nm for 3Y-ZrO_2). For the 8Y-ZrO_2, HRTEM reveals a quite similar nanocrystal morphology to 1.5Y-ZrO_2 and 3Y-ZrO_2, with particles fully crystallized (Figure 7c). Nevertheless, if the average nanocrystal size estimated is still of 7 ± 2 nm, a broader size distribution is observed, with particle size ranges from 3.5 to 12 nm (Figure 7d). Moreover, some particles exhibit a more oval morphology that could reflect a preferential particle growth axis for this higher yttrium content under the synthesis conditions, but which is not studied in the framework of this study.

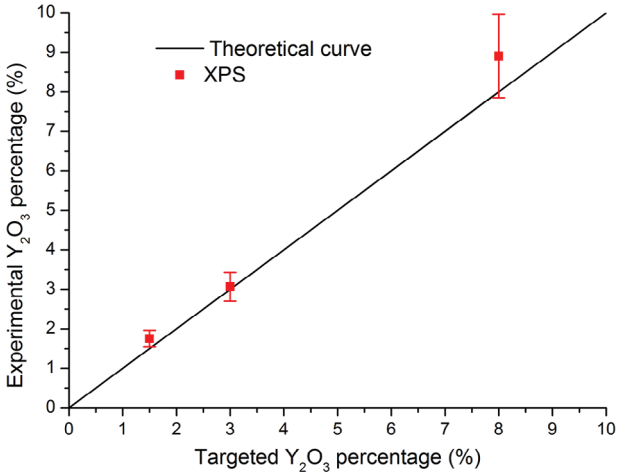

Figure 6. Experimental Y_2O_3 atomic percentage obtained by XPS compared to the targeted percentage.

Overall, these microstructural analyses confirm the high potential of the sol–gel like method in supercritical fluid media for the production of high-quality nanocrystals with an average particle size centered at 7 nm associated with a narrow size distribution, whatever the yttrium content. The slight change in morphology of particles observed with the increase of yttrium content needs to be confirmed, as well as a possible relationship with the particle growth mechanism.

2.2.3. Structural Analyses

1.5Y-ZrO_2: The Rietveld refinement of the room temperature Cu-PXRD pattern measured on the 1.5Y-ZrO_2 powder reveals that both the tetragonal and the monoclinic structures are present. They can be clearly observed despite the peak broadening arising from nanosized crystallites. It is then possible to estimate an approximative amount of 15 wt. % of monoclinic phase (**Figure** 8a) in this powder. The Raman spectrum of the 1.5Y-ZrO_2 highlights the structural changes according to the substitution rate and confirms the presence of the two phases revealed by Cu-PXRD patterns and its Rietveld refinement (Figure 8b). The two main bands at 178 and 190 cm^{-1} characteristics of the monoclinic structure are observed, as well as the other ones located at 219,

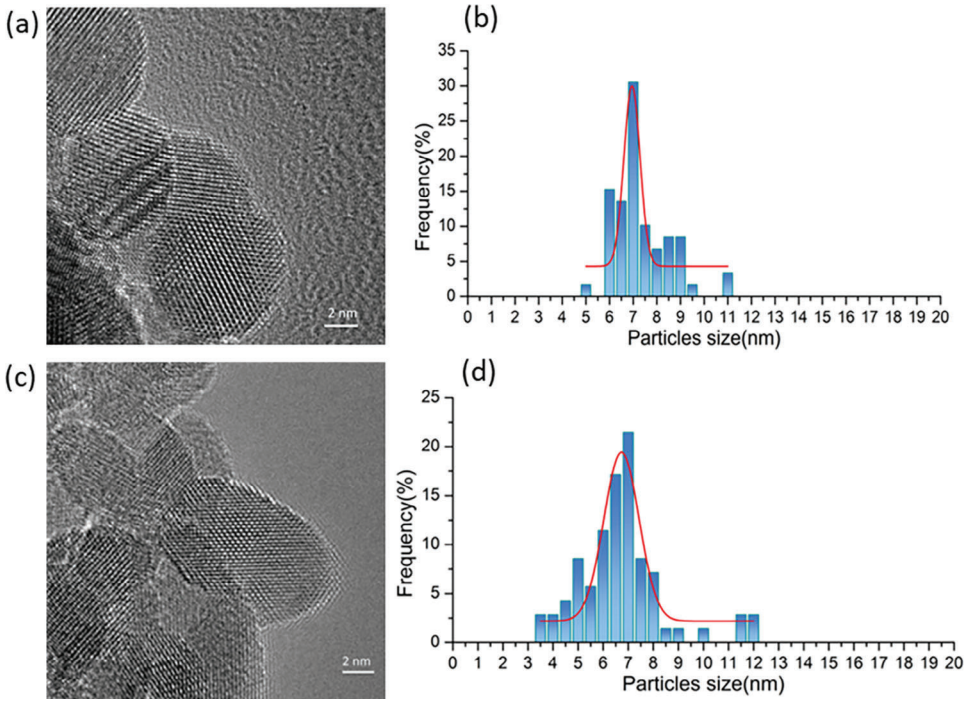

Figure 7. a) HRTEM of the 1.5Y-ZrO_2 particles, b) Size distribution of the 1.5Y-ZrO_2 particles, c) HRiTEM of the 8Y-ZrO_2 particles, d) Size distribution of the 8Y-ZrO_2 particles.

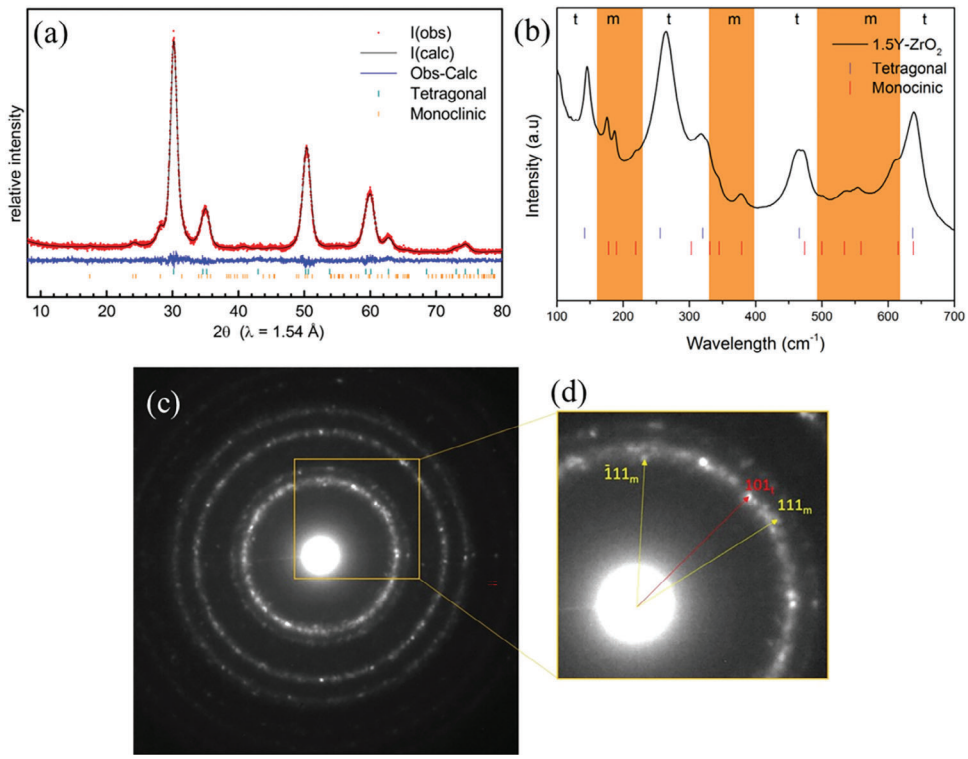

Figure 8. a) Rietveld refinement of 1.5Y-ZrO_2 powder for 2θ range from 8° to 80°, b) Raman spectra of 1.5Y-ZrO_2 powder collected at room temperature in the 100–700 cm^{-1} domain. The monoclinic (m) and tetragonal (t) are separated by the orange areas, respectively. c) SAED pattern of a large number of nanocrystals. d) Zoom of the SAED pattern showing the presence of both the tetragonal and monoclinic symmetries.

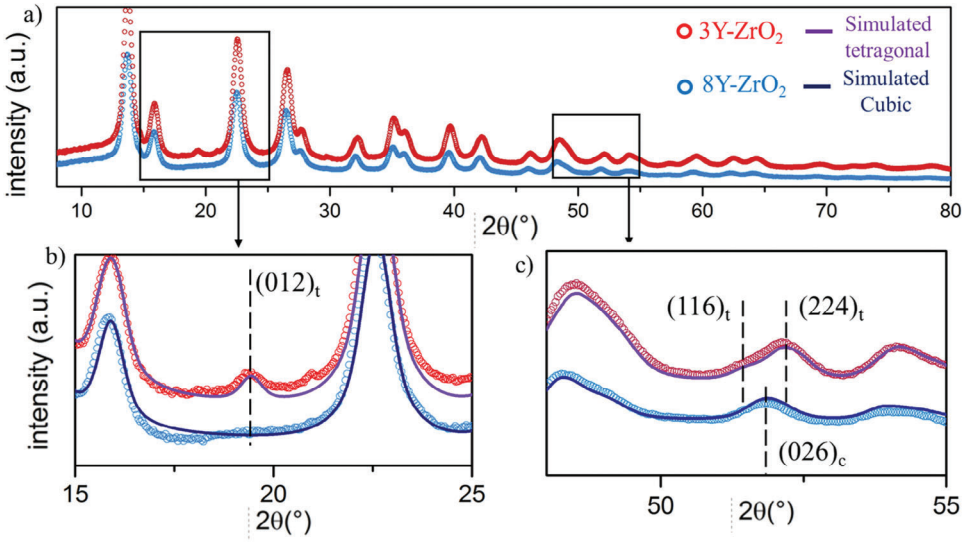

Figure 9. a) High energy Mo-PXRD patterns for the samples 3Y-ZrO_2 and 8Y-ZrO_2, plotted as the square root of measured intensity versus 2θ, b) overlaid experimental data (open circles) and simulated PXRD patterns (solid lines) in the zoomed 2θ range 15° to 25°, and similarly c) in the zoomed 2θ range 48° to 55°.

345, 379, 500, 534, 555 and 610 cm^{-1}. A monoclinic content of 9 wt% is calculated (equation S2, Supporting Information), this value is a bit lower than the one evaluated by Rietveld refinement (i.e., 15 wt%) but the difference remains reasonable and estimate an overall quantity of monoclinic phase ≈10 wt%. SAED patterns were obtained on the 1.5Y-ZrO_2 sample (Figure 8c). It can clearly be observed that the first ring is broader than the next ones. Indeed, this observation can be explained by the superposition of reflections coming from both tetragonal and monoclinic symmetries as shown on the zoom of the first ring (Figure 8d).

These results follow the established trend showing a monoclinic phase content intermediate between that reported for undoped ZrO_2 nanocrystals (i.e., 40 wt%),[17] and the 0 wt% obtained for the 3Y-TZ, all produced under the exact same synthesis conditions (excepting the yttrium content). Such results show that the solvothermal synthesis process of low-yttria doped zirconia is suitable for synthesizing fully crystallized nanoparticles showing an important quantity of metastable t-phase.

8Y-ZrO_2: The high energy Mo-PXRD measurements performed with long collection times were able to better resolve weak intensity peaks. Nevertheless, the distinction between cubic and tetragonal ZrO_2 polymorphs can be difficult to achieve with PXRD. This is even more challenging in the case of nanoscale crystallite domains, as inherent Bragg peak broadening effectively prevents the observation of most splitting of the hkl reflections associated with the lower symmetry tetragonal unit cell. However, on high quality data, small features in the diffraction patterns can be used to evaluate the structural features even in the case of nano powders. **Figure** 9a shows the full range of the Mo-PXRD data for 3Y-ZrO_2 and 8Y-ZrO_2 samples, revealing the overall very similar diffraction patterns. Nevertheless, a zoom of both patterns (Figure 9b) shows the presence of an extra weak peak in the 3Y-ZrO_2 sample, which corresponds to the hkl (012) reflection of the tetragonal $P4_2/nmc$ cell. This reflection is not due to lattice changes, but rather originates with subtle oxygen displacements along the c axis from the ideal anion site in the fluorite-type cubic. This reflection is forbidden in the fluorite-type $Fm3m$ cubic ZrO_2 structure. This presence and intensity of this (012) peak has been previously used with neutron powder diffraction to quantity the boundary around the cubic and tetragonal phase transition in ZrO_2-Y_2O_3 solid solutions.[36] In our study, simulated PXDR patterns overlaid on experimental data (Figure 9), reveal how this feature can be used with high quality X-ray data to distinguish between cubic and tetragonal ZrO_2 polymorphs. Additionally, small peak position shifts at high 2θ values can be also observed (Figure 9c**)**. These shifts result from a subtle change in the unit cell c/a axial ratio, where an axial ratio > 1.0 indicates a tetragonal type elongation along the c-axis direction.

A detailed examination of the tetragonal and cubic phase boundary in yttria-doped zirconia is beyond the scope of the current study. However, based on a qualitative examination of high-quality X-ray data, it is possible to evaluate the presence of signature features associated with a tetragonal $P4_2/nmc$ type structure. For the nanoscale powders examined here, it is estimated that average oxygen position shifts of 0.1 Å (equivalent to a factional z-shift of 0.02) and c/a axial ratio distortions greater than 1.01 can be detected. Below these detection limits for the PXDR data of the current study, as in the case on the 8Y-ZrO_2 sample, the average structure from these Mo-PXRD data can be considered indistinguishable from that of a pseudo-fluorite type cubic ZrO_2 phase.

For the simulated $P4_2/nmc$ pattern, the tetragonal c/a ratio is 1.015 with an oxygen site displacement of 0.2 Å along the z direction.

The Raman spectra for the 8Y-ZrO_2 sample (**Figure 10**) shows a significant decrease in the relative intensity of every bands due to the change of symmetry, reflecting the higher symmetry of the cubic structure. In addition, the disappearance of the band at 320 cm^{-1} and the shift to a lower values of the bands at 637 to 620 cm^{-1} are two features supporting the stabilization of the cubic structure.[25] If it cannot be firmly stated that there is no contribution of the tetragonal phase, these changes are in good

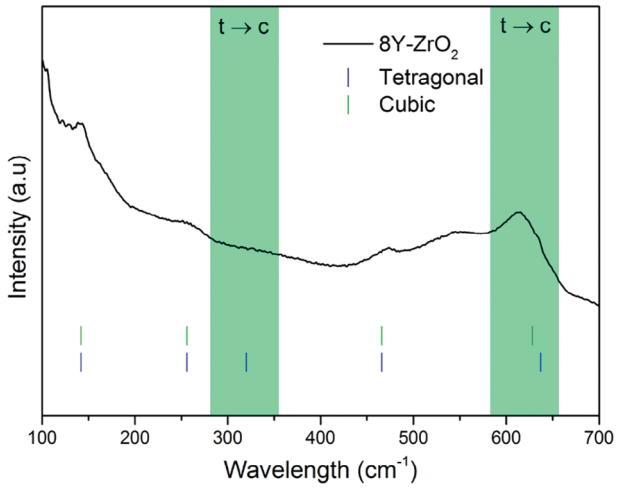

Figure 10. Raman spectra of 8Y-ZrO_2 powder collected at room temperature in the 100–700 cm^{-1} domain with domains characteristic of the tetragonal to cubic transition are highlighted with the green bands.

agreement with the Mo-PXRD observations, indicating as well a pseudo-cubic structure, which in agreement with the expected one in the ZrO_2-Y_2O_3 phase diagram.[26]

To go further into the analysis of the 8Y-ZrO_2 sample, SAED showed the presence of two types of patterns (**Figure 11**). On the first one, a limited number of rings are observed. These reflections are consistent with a cubic symmetry. On the second one, additional reflections appear, indicating the existence of the tetragonal phase. It can therefore be concluded that the two symmetries (i.e., cubic and tetragonal) co-exist in the 8Y-ZrO_2 powder. This could indicate that for high Y_2O_3 content, its distribution withing the particles is less homogeneous, i.e., area with richer content will lead to the stabilization of the cubic phase while area with lower content will lead to the stabilization of the tetragonal one.

These last results are consistent with the pseudo cubic structure determined by Mo-PXRD and Raman spectroscopy. Nevertheless, SAED patterns showed that some local co-existence of both cubic and tetragonal symmetries must be considered. It still highlights the feasibility to stabilize a mostly cubic structure in 8Y-ZrO_2 even for such small particles size. The structural properties of zirconia were shown to be mainly controlled by the structural disorder around the oxygen vacancies.[19] To achieve full stability of the cubic phase, the electrostatic neutrality should be maintained by a large concentration of oxygen vacancies leading to the distortion of the oxygen sublattice. In-depth investigations would contribute to better understand how the lattice accommodates such content of oxygen vacancies in the 7 nm-sized 8Y-ZrO_2 nanoparticles obtained in sol–gel like supercritical conditions but this is beyond the scope of this study.

3. Conclusion

In the present study we demonstrate for the first time the interest of using supercritical sol–gel like synthesis for the continuous production of high quality ZrO_2 nanocrystals stabilized with different amounts of Y_2O_3. The flexibility of this approach enabling to tune the stabilized polymorphs and mixture of them by adjusting the Y_2O_3 content from 1.5 up to 8 mol.%, while keeping all the other synthesis parameters constant, was highlighted. When doping with 1.5 mol.% of Y_2O_3 (1.5Y-ZrO_2), a mixture of tetragonal and monoclinic phases was obtained but with 90 wt% of tetragonal phase. Increasing the Y_2O_3 content up to 3 mol.% (3Y-ZrO_2) allowed the synthesis of nanocrystals with 100 wt% of tetragonal phase. A further increase to 8 mol.% of Y_2O_3 (8Y-ZrO_2) lead to the stabilization of a pseudo cubic structure with a low fraction of tetragonal particles. Whatever the composition of the as-synthesized powder, well-crystallized nanoparticles of 7 nm in size were obtained. In conclusion, the fine tuning over the yttrium content is thus the indirect key controlling the produced polymorphism. This continuous flow solvothermal or sol-gel like supercritical synthesis enables a unique fine structural control for such small yttria-doped zirconia nanocrystals, which was not reported yet to the best of our knowledge.

4. Experimental Section

Materials: Zirconium (IV) propoxide solution, 70 wt% in 1-propanol (Sigma–Aldrich), Yttrium 2-methoxyethoxide solution, 15–20 wt% in 2-methoxyethanol (Sigma–Aldrich), absolute ethanol (Sharlau ≥ 99.9%) and deionized water were used as received. Three precursor solutions in ethanol were prepared (10^{-2} M) of composition 1.5, 3 and 8 mol.% of Y_2O_3 (1.5Y-ZrO_2, 3Y-ZrO_2 and 8Y-ZrO_2, respectively). A commercial 3Y-TZ powder (US research nanomaterials 3Y-ZrO_2) with particle an average particle size of 40 nm and a ratio of 90 wt% of tetragonal phase and 10 wt% of the monoclinic one was used as reference.

Yttria-Stabilized Zirconia Solvothermal Synthesis: Yttria-stabilized zirconia nanoparticles were synthesized using a continuous flow reactor as described in **Figure 12**. Two high-pressure pumps (HPP) allowed to feed the reactor with a precursor solution (10^{-2} M precursor in ethanol) and deionized water to reach a mass ratio of 50/50 water/ethanol. Distilled water is first preheated at 250 °C using a 6 m coiled 1/8 tubing in 316 stainless steel (SS-316) inserted inside a heating clamp allowing a temperature at the mixing point with the precursor solution line at 150 °C. Then the reactor or "hot zone" consisted of a coiled 24 m long 1/8 in SS-316 tubing inserted inside another heating clamp to control the reaction temperature (T = 400 °C) along the 24 m tubing. The quenching of nanoparticle growth was performed by flowing the suspension through an ice-cooled 1/8 in SS-316 tubing downstream the reactor prior to recover it at the outlet of the reactor. All along the synthesis process, the reactor was held at a constant pressure of 25 MPa using a back-pressure regulator (BPR). Finally, as-synthesized nanoparticles were separated from the solvent mixture by filtration, washed with ethanol and dried at room temperature.

Note that the critical parameters of a 50/50 wt% water–ethanol mixture are T_{crit} = 279.9 °C and p_{crit} = 10.6 MPa,[37] which means that the oxide particles prepared during this study were indeed synthesized in supercritical conditions. In the following, this process would be called "supercritical solvothermal synthesis" but also "sol–gel route under supercritical conditions". Indeed, a homogeneous solution of precursors dissolved in ethanol was mixed with preheated water that triggers the conventional sol-gel like reaction. Once inside the reactor and under supercritical conditions, the drop in dielectric constant of the solvent mixture force the burst nucleation, enabling a single step synthesis of fully crystallized nanoparticles without any post heat treatment.

Characterization of As-Synthesized Yttria-Stabilized Zirconia Powders: Powder X-ray diffraction data was collected at room temperature using a Bragg–Brentano geometry (PANalytical X'Pert MPD Pro diffractometer) with Cu Kα source (λ = 1.54 Å) and a secondary monochromator was used. Measurements were performed with a 2θ step size of 0.0167° over the 2θ range 10–120°. Additional X-ray analysis on selected samples was

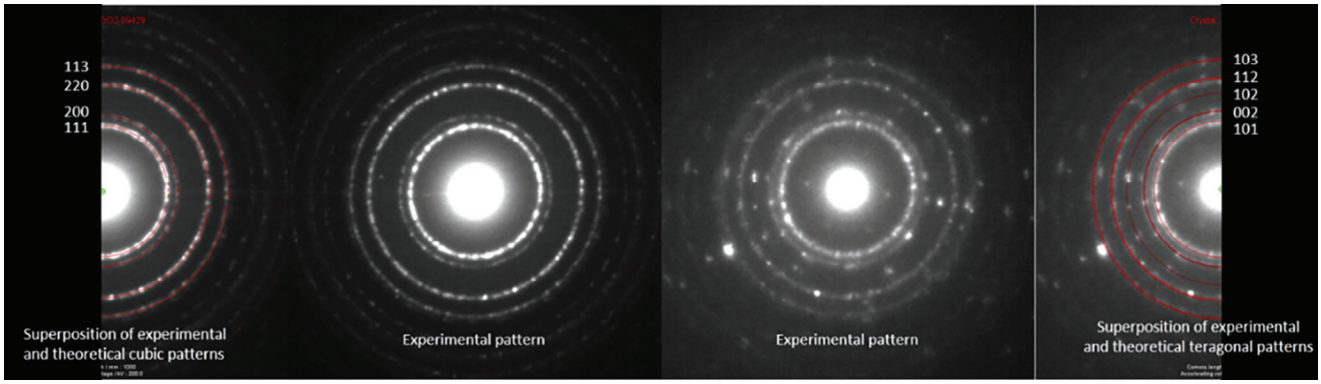

Figure 11. Two types of SAED patterns observed on the 8Y-ZrO_2 powder. The left pattern is consistent with a cubic cell, on the right additional reflections are consistent with a tetragonal symmetry.

performed using a capillary Debye Scherrer geometry (Bruker D8 Discover Diffractometer) with a Mo source (λ = 0.71 Å) and a DECTRIS EIGER2 500K detector. By the use of a variable collection time strategy optimizing high angle counting statistics, total scattering data up to a Q_{max} of ≈17 $Å^{-1}$ suitable for Pair Distribution Function analysis was obtained. Rietveld refinements of as-measured Mo-PXRD data were performed with the DIFFRAC.TOPAS software package using a Fundamental Parameters (FP) approach for the instrumental contribution. Sample microstructure effects were fit with Lorentzian crystallite size terms using an integral breadth based. Conversion of the measured Mo source total scattering data to a PDF reduced pair distribution function G(r) was performed using the PDFgetX3 software package.[38] Small-box structural fits to the resulting real-space G(r) functions were subsequently performed with the DIFFRAC.TOPAS (v6) software package.

For further structural characterization of the as-synthesized powders, room temperature Raman spectra were collected with λ_{exc} = 532 nm in a backscattering geometry equipped with an Andor CCD detector (XploRA HORIBA Scientific Raman spectrometer). Data were collected with a resolution of 4 cm^{-1} over the 100–800 cm^{-1} domain and were further integrated using the LABSPEC software. Phases quantifications was determined using the method developed by Kim et al..[39] The tetragonal/monoclinic phase ratio is determined by computing the intensity ratio x_m of the two monoclinic peaks at 180 and 192 cm^{-1} and the intensity of the tetragonal peak located at 148 cm^{-1}. Then the volume and mass ratios could be computed.

Microstructural features were characterized using High-Resolution Transmission Electron Microscopy (JEOL 2200 FS microscope equipped with a Gatan Ultrascan CCD 2k–2k camera) coupled with Energy Dispersive X-ray Spectroscopy (EDS also known as EDX analysis). Prior to their observation, powders were dispersed in absolute ethanol and sonicated for 15 min. The samples were prepared by casting two small drops of the diluted nanoparticle suspension on a carbon-coated copper grid and air-drying. Then two drops were casted on a TEM copper grid covered with a carbon lacey film. Chemical mapping was obtained with a spot size of 1 nm and a drift correction every 10 s. Selected Area Electron Diffraction patterns were also obtained (JEOL 2100 microscope equipped with a GATAN Orius 200D camera). To obtain crystallographic information on one single nanocrystal (i.e., nanodiffraction), a slightly convergent beam of ≈5 nm in diameter was used. The average particle size was determined using ImageJ software, measuring at least 50 particles. The size distribution was estimated using the standard deviation of the measured sizes.

Surface properties of the as-synthesized samples were investigated by Fourier Transform Infrared (FTIR) spectroscopy (Bruker equinox 55 spectrophotometer). The nanoparticles were grounded, dispersed into a KBr matrix and shaped into pellets prior to measurements. A total of 32 scans was realized for each sample in the 400 and 4000 cm^{-1} spectral absorption domain using a global radiation source, and the spectral resolution was 4 cm^{-1}. X-ray Photoelectron Spectroscopy was also used as complementary technique (ThermoFisher Scientific K-ALPHA spectrometer) with a monochromatized Al-Kα source ($h\nu$ = 1486.6 eV) and a 400 µm X-ray spot size. Prior to XPS characterization, the powders were pressed into high purity indium foils. The full spectra (0–1150 eV) were obtained with a constant pass energy of 200 eV, while high-resolution spectra were recorded with a constant pass energy of 40 eV. Charge neutralization was applied during the analysis and depth profiles were fulfilled with an Ar^+ ion gun. High resolution spectra (i.e., C1s, O1s, Zr3d, Y3d, ...) were quantified using the AVANTAGE software provided by ThermoFisher Scientific by applying Scofield sensitivity factors. All spectra were shifted versus C1s

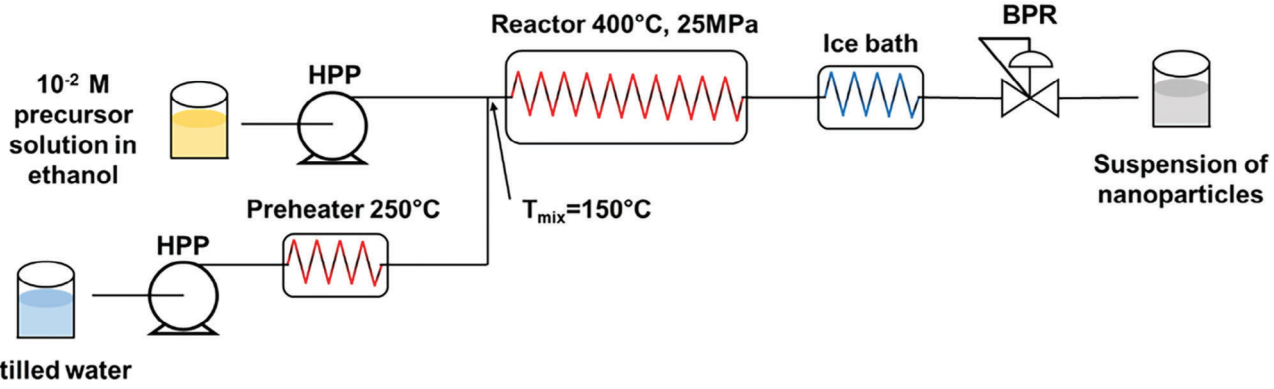

Figure 12. Continuous flow set-up used in this study for the synthesis of xY_2O_3-ZrO_2 nanoparticles (x = 1.5, 3, and 8 mol.% Y_2O_3). HPP stands for high pressure pump and BPR for back pressure regulator.

main peak at 285 eV leading to a $Zr3d_{5/2}$ binding energy ≈182.0 eV. Main attention was paid on O1s spectra (before etching) to get proportions of each oxygen environment after fitting. Quantification is based on calculating the area of high-resolution spectra, which are corrected using theoretical photoemission sensitivity coefficients. Hence, this method induces an uncertainty of 10% in average.

Supporting Information

Supporting Information is available from the Wiley Online Library or from the author.

Acknowledgements

This work had been made possible by the financial support of the ANR project DIPLOMAT (ANR-21-CE08-0024), the Université de Bordeaux, the Région Nouvelle Aquitaine and the CNRS. The authors wish to thank the University of Bordeaux for funding this research and in particular the Ph.D. grant of Y.D.

Conflict of Interest

The authors declare no conflict of interest.

Data Availability Statement

The data that support the findings of this study are available from the corresponding author upon reasonable request.

Keywords

nanocrystals, sol–gel, supercritical solvothermal synthesis, yttria-stabilized zirconia

Received: September 5, 2023
Revised: November 24, 2023
Published online:

[1] C. Ricca, A. Ringuedé, M. Cassir, C. Adamo, F. Labat, *J. Comput. Chem.* **2015**, *36*, 9.
[2] R. C. Garvie, R. H. Hannink, R. T. Pascoe, *Nature* **1975**, *258*, 703.
[3] J. Chevalier, L. Gremillard, A. V. Virkar, D. R. Clarke, *J. Am. Ceram. Soc.* **2009**, *92*, 1901.
[4] O. Akhlaghi, E. Camposilvan, Z. Goharibajestani, S. K. Abkenar, C. W. Ow-Yang, Y. Jorand, L. Gremillard, V. Garnier, J. Chevalier, *J. Eur. Ceram. Soc.* **2022**, *42*, 7187.
[5] H. Guo, J. Guo, A. Baker, C. A. Randall, *J. Am. Ceram. Soc.* **2017**, *100*, 491.
[6] N. Kumari, S. Sareen, M. Verma, S. Sharma, A. Sharma, H. S. Sohal, S. K. Mehta, J. Park, V. Mutreja, *Nanoscale Adv* **2022**, *4*, 4210.
[7] L. Liu, S. Wang, G. Jiang, B. Zhang, J. Yang, J. Wang, W. Liu, Y. Li, H. Liu, *Ceram. Int.* **2022**, *48*, 32649.
[8] A. H. Heuer, R.-R. Lee, *Rev. Phys. Appliquée* **1988**, *23*, 565.
[9] M. W. Pitcher, S. V. Ushakov, A. Navrotsky, B. F. Woodfield, G. Li, J. Boerio-Goates, B. M. Tissue, *J. Am. Ceram. Soc.* **2005**, *88*, 160.
[10] M. Tsang, G. Philippot, C. Aymonier, G. Sonnemann, *Green Chem.* **2016**, *18*, 4924.
[11] C. Aymonier, G. Philippot, A. Erriguible, S. Marre, *J. Supercrit. Fluids* **2018**, *134*, 184.
[12] J. Becker, P. Hald, M. Bremholm, J. S. Pedersen, J. Chevallier, S. B. Iversen, B. B. Iversen, *ACS Nano* **2008**, *2*, 1058.
[13] M. Bremholm, J. Becker-Christensen, B. B. Iversen, *Adv. Mater.* **2009**, *21*, 3572.
[14] C. Tyrsted, B. R. Pauw, K. M. Ø. Jensen, J. Becker, M. Christensen, B. B. Iversen, *Chem. – Eur. J.* **2012**, *18*, 5759.
[15] A. C. Dippel, K. M. Jensen, C. Tyrsted, M. Bremholm, E. D. Bojesen, D. Saha, S. Birgisson, M. Christensen, S. J. L. Billinge, B. B. Iversen, *Acta Crystallogr. Sect. Found. Adv.* **2016**, *72*, 645.
[16] L. Liu, S. Wang, B. Zhang, G. Jiang, J. Yang, Y. Li, W. Liu, J. Wang, W. Kong, *Ceram. Int.* **2022**, *48*, 4401.
[17] A. Auxéméry, G. Philippot, M. R. Suchomel, D. Testemale, C. Aymonier, *Chem. Mater.* **2020**, *32*, 8169.
[18] M. Bondesgaard, J. Becker, J. Xavier, H. Hellstern, A. Mamakhel, B. B. Iversen, *J. Supercrit. Fluids* **2016**, *113*, 166.
[19] S. Fabris, *Acta Mater.* **2002**, *50*, 5171.
[20] B. Basu, J. Vleugels, O. V. D. Biest, *Mater. Sci. Eng. A* **2004**, *366*, 338.
[21] G. Roebben, B. Basu, J. Vleugels, O. Van der Biest, *J. Eur. Ceram. Soc.* **2003**, *23*, 481.
[22] F. Zhang, H. Reveron, B. C. Spies, B. Van Meerbeek, J. Chevalier, *Acta Biomater.* **2019**, *91*, 24.
[23] I. Gonzalo-Juan, B. Ferrari, M. T. Colomer, M. A. Rodriguez, A. J. Sanchez-Herencia, P.-Y. Koh, A. S. Teja, *Mater. Chem. Phys.* **2012**, *134*, 451.
[24] P. Bouvier, E. Djurado, G. Lucazeau, T. Le Bihan, *Phys. Rev. B* **2000**, *62*, 8731.
[25] C. Wulfman, M. Sadoun, M. Lamy De La Chapelle, *IRBM* **2010**, *31*, 257.
[26] R. A. Miller, J. L. Smialek, R. G. Garlick, *Adv. Appl. Ceram.* **1981**, *3*, 241.
[27] H. Reverón, C. Aymonier, A. Loppinet-Serani, C. Elissalde, M. Maglione, F. Cansell, *Nanotechnology* **2005**, *16*, 1137.
[28] H. Reverón, C. Elissalde, C. Aymonier, O. Bidault, M. Maglione, F. Cansell, *J. Nanosci. Nanotechnol.* **2005**, *5*, 1741.
[29] G. Philippot, K. M. Ø. Jensen, M. Christensen, C. Elissalde, M. Maglione, B. B. Iversen, C. Aymonier, *J. Supercrit. Fluids* **2014**, *87*, 111.
[30] G. Philippot, M. Albino, U.-C. Chung, M. Josse, C. Elissalde, M. Maglione, C. Aymonier, *Mater. Des.* **2015**, *86*, 354.
[31] G. Philippot, E. D. Boejesen, C. Elissalde, M. Maglione, C. Aymonier, B. B. Iversen, *Chem. Mater.* **2016**, *28*, 3391.
[32] W. Zhu, S. Nakashima, M. Matsuura, H. Gu, E. Marin, G. Pezzotti, *J. Eur. Ceram. Soc.* **2019**, *39*, 4928.
[33] W. Zhang, Z. Wang, J. Huang, Y. Jiang, *Energy Fuels* **2021**, *35*, 9209.
[34] K. Tomishige, Y. Ikeda, T. Sakaihori, K. Fujimoto, *J. Catal.* **2000**, *192*, 355.
[35] E. Roitero, H. Reveron, L. Gremillard, V. Garnier, C. Ritzberger, J. Chevalier, *J. Eur. Ceram. Soc.* **2023**, *43*, 2852.
[36] M. Yashima, S. Sasaki, M. Kakihana, Y. Yamaguchi, H. Arashi, M. Yoshimura, *Acta Crystallogr. B* **1994**, *50*, 663.
[37] A. A. Abdurashidova, A. R. Bazaev, E. A. Bazaev, I. M. Abdulagatov, *High Temp.* **2007**, *45*, 178.
[38] P. Juhás, T. Davis, C. L. Farrow, S. J. L. Billinge, *J. Appl. Crystallogr.* **2013**, *46*, 560.
[39] B.-K. Kim, J.-W. Hahn, K. R. Han, *J. Mater. Sci. Lett.* **1997**, *16*, 669.